The effect of nacelle-to-rotor size on the wake of a miniature wind turbine

Journal of Physics: Conference Series **2767** (2024) 092057 doi:10.1088/1742-6596/2767/9/092057

The effect of nacelle-to-rotor size on the wake of a miniature wind turbine

Arslan Salim Dar, Rim Majzoub and Fernando Porté-Agel

Wind Engineering and Renewable Energy Laboratory (WIRE), École Polytechnique Fédérale de Lausanne (EPFL), 1015 Lausanne, Switzerland

E-mail: arslan.dar@epfl.ch; fernando.porte-agel@epfl.ch

Abstract. Wind tunnel experiments are performed to investigate the effect of nacelle-to-rotor size on the wake of a wind turbine under different Reynolds numbers. Four different turbine configurations are tested, which vary in the rotor diameter and nacelle length and diameter. The near wake region is observed to be significantly affected by the nacelle-to-rotor size of the turbine. The difference in the averaged streamwise velocity and streamwise turbulence intensity is affected more by the change in the rotor diameter than by the change in the nacelle diameter. This is likely due to the change in the nacelle length to rotor diameter ratio, and the change in the distance between the ground and rotor lower tip. The differences in the near wake characteristics are reduced by the increase in the Reynolds number. The onset of the far wake is unaffected by the nacelle-to-rotor size, and consequently, the far wake modeling can be performed with good accuracy using existing analytical models. The power coefficient values show an improvement with the increase in the Reynolds number due to the higher efficiency of the rotor and motor.

1. Introduction

Wind turbines interact with the atmospheric boundary layer to extract energy and generate a low-speed and high-turbulence region behind them, known as the wake. Wind turbine wakes are highly complicated and their characteristics are dependent on the aerodynamic properties of the turbine, atmospheric conditions, and surface characteristics [1]. Wind tunnel experiments using miniature wind turbines offer a unique capability to understand wind turbine wake and power characteristics under controlled and reproducible conditions [2]. In addition to unraveling the flow physics, wind tunnel experiments are commonly used as benchmarks to test and validate numerical models [3].

Wind tunnel experiments, however, have certain limitations, such as the Reynolds number being comparatively smaller, and the nacelle-to-rotor diameter ratio being comparatively larger than those for the utility-scale turbines. For miniature wind turbines, the ratio between nacelle-to-rotor diameter is usually in the range of 0.06-0.18 [3–9]. For utility-scale turbines, on the other hand, this ratio is typically less than 0.05 [2, 9–11]. Similarly, the ratio of nacelle length to rotor diameter is typically greater than 0.2 for miniature wind turbines [4–6, 12], whereas it is less than 0.1 for utility-scale turbines [11].

Several studies have investigated the effect of the nacelle and tower on the wake of a wind turbine. Santoni et al. [13] showed that the turbine nacelle and tower produce an added velocity deficit and increase the mean kinetic energy flux in the wake. They also concluded that modeling

the nacelle and tower of a turbine is important for an accurate representation of wake recovery and kinetic energy entrainment. Abraham et al. [10] investigated the effect of nacelle and tower on the near wake of a utility-scale turbine. They found that the nacelle leads to flow acceleration around it and the tower leads to a velocity reduction, which results in an asymmetric velocity deficit profile in the near wake. In addition, they found high turbulence kinetic energy in the regions of high shear surrounding the nacelle and blade tips. De Cillis et al. [14] performed a proper orthogonal decomposition analysis of the wake of a turbine with and without the effect of the nacelle and tower. They showed that the presence of the nacelle and tower leads to the generation of low-frequency modes in the near wake, which play a role in the recovery of the wake. Guo et al. [15] performed a field study on the effect of nacelle and tower on the wake of a wind turbine. They observed an increase in the velocity deficit and turbulence kinetic energy in the near wake due to the effect of the nacelle and tower. Several other studies [16, 17] also made similar observations regarding the effect of the nacelle on the wake deficit and turbulence kinetic energy in the near wake. Zhu et al. [18] performed a dynamic mode decomposition analysis on the turbine wake with and without the tower and nacelle. They showed that the vortices shed by the nacelle and tower can distort the helical vortex filament of the tip vortices. Dar and Porté-Agel [19] also showed that the hub vortex can affect the development of tip vortices in complex flow conditions.

Although the above-mentioned studies have highlighted several important changes in the wake flow induced by the nacelle of a turbine, it is not well understood how the size of the nacelle relative to the rotor size can influence the wake of a turbine. Answering this question is important, especially for miniature wind turbines due to their relatively large nacelle sizes compared to the utility-scale ones. More specifically, we are interested in understanding whether the size of the nacelle has an impact on the far wake of a wind turbine, as it is the region where most downstream turbines are located, and thus the region of interest from the perspective of resource assessment and layout optimization of a wind farm. The current study intends to identify the differences and similarities in the wake of a wind turbine with different combinations of nacelle-to-rotor sizes under different Reynolds numbers. For this purpose, wind tunnel experiments are performed using particle-image velocimetry. In addition, the power extracted by the turbine is also measured and the power coefficient is compared between different cases. The rest of the article is structured as follows: the details of the experiments and turbine configurations are given in section 2; the results from the study are presented and discussed in section 3; and finally, some concluding remarks are given in section 4.

2. Experimental Setup

The experiments were performed in the boundary layer wind tunnel at the WiRE laboratory of EPFL. The wind tunnel is a closed-loop type and the flow is driven by a 130 kW fan. The test section has the dimensions of 28 m $\times$ 2.6 m $\times$ 2 m (length $\times$ width $\times$ height) with a contraction of 5:1 area ratio before the inlet of the test section. The flow is conditioned through a series of meshes and honeycomb screens before the contraction to achieve a uniform and low-turbulence flow at the entrance of the test section. Due to the long fetch of the test section, a turbulent boundary layer develops naturally on the smooth floor of the tunnel. The experiments are performed at approximately 22 m downstream from the inlet where the boundary layer is fully developed.

A three-bladed horizontal axis wind turbine WiRE-01 was used in this study [20]. The blade has a circular arc shape with 5% camber and 5% thickness with respect to the chord length. Two different scalings of the rotor were used: one with a rotor diameter d of 15 cm and the other with a rotor diameter of 10.5 cm. Both rotors have a thrust coefficient of around 0.8 [5, 6] at the optimal tip speed ratio. The nacelle has a direct current (DC) motor used to control the turbine rotation and measure the power produced by it. Two different DC motors were used to

model different nacelle sizes, both produced by Maxon motors. The first nacelle configuration consists of a DC motor DCX10L along with a digital encoder ENX10 with a diameter d_N of 1 cm and a length l_N of 4.5 cm, whereas the second configuration consists of a DC motor DCX16L along with the same digital encoder, which results in a diameter of 1.6 cm and a length of 5.5 cm. Four different turbine configurations were made using the two different rotor and nacelle sizes described above. The turbine hub height z_h with the DCX10L motor is 12.5 cm, whereas it is 12.8 cm with the DCX16L motor.

The flow measurements were performed using a two-dimensional two-component particle-image velocimetry (2D2C-PIV) system in a vertical plane passing through the turbine center. The PIV system comprises an sCMOS camera (2560 × 2160 pixels), a 425 mJ Nd:YAG dual-head laser, and a programmable timing unit. The images are captured at a rate of 10 Hz, where 1000 instantaneous flow fields are used to obtain time-averaged flow statistics. The power P produced by the turbine was measured through the direct current motor that serves as the nacelle of the turbine. The turbine power output is computed as:

$$P = (Q_{sh} + Q_f)\Omega = (KI + Q_f)\Omega, \tag{1}$$

where Q_{sh} is the shaft torque, K is the torque constant of the motor, I is the current generated by the turbine, Q_f is the frictional torque, and Ω is the rotational speed of the rotor. The frictional torque Q_f measured by Bastankhah & Porté-Agel [20] as a function of rotational speed is used for the respective motors. Power measurements were performed at a sampling rate of 1 kHz for a sampling duration of 140 s.

Four different boundary layers were generated to obtain two comparable Reynolds numbers with respect to the rotor diameter: $Re = \frac{\overline{u_h} d}{\nu}$, where $\overline{u_h}$ is the hub height time-averaged streamwise velocity, d is the rotor diameter and ν is the kinematic viscosity of air. Figure 1 compares the characteristics of all the turbulent boundary layers. It is to be noted that the height coordinate is normalized by the boundary layer height δ in figure 1. This is done to compare different boundary layers without the influence of turbine dimensions. It can be observed that the turbine is always immersed in the boundary layer. The normalized averaged streamwise velocity is comparable between different boundary layers. The streamwise turbulence intensity is computed as $I_u = \sigma_u/\overline{u_h}$, where σ_u is the standard deviation in streamwise velocity. The streamwise turbulence intensity at the hub height is in the range of 6.5%-7.1% for different boundary layers, with an almost linear decrease with height. The normalized averaged momentum flux $\overline{u'w'}/\overline{u_h}$ is also comparable between different boundary layers, with a high magnitude close to the surface due to high shear. A logarithmic fit according to $\overline{u} = \frac{u_*}{\kappa} ln(\frac{z}{z_0})$, where u_* is the friction velocity, κ is the von Karman constant assumed to be 0.4 and z_0 is the aerodynamic roughness length, is performed on the lowest 15% of the boundary layer. The normalized averaged streamwise velocity along with the logarithmic fit are shown in figure 1 (d). As can be seen, all boundary layers show comparable profiles. A full description of the turbine configurations along with characteristic flow parameters is shown in table 1.

Turbine	d (cm)	z_h (cm)	d_N (cm)	l_N (cm)	$\frac{d_N}{d}$ (%)	$\frac{l_N}{d}$	$\overline{u_h}$ (ms^{-1})	δ (cm)	u_* (ms^{-1})	z_0 (m)	Re
R15-M1	15	12.5	1	4.5	6.7	0.3	4.3	35	0.23	6.2×10^{-5}	41300
R10.5-M1	10.5				9.5	0.43	6.5	34.6	0.31	2.4×10^{-5}	43500
R15M-1.6	15	12.8	1.6	5.5	10.7	0.36	4.3	35	0.23	6.2×10^{-5}	41300
R10.5-M1.6	10.5				15.2	0.52	6.5	34.6	0.31	2.4×10^{-5}	43500
R15-M1.6 High Re	15				10.7	0.36	7.9	33.8	0.43	1.1×10^{-4}	75000
R10.5-M1.6 High Re	10.5				15.2	0.52	9.92	34.4	0.59	1.3×10^{-4}	67000

Table 1. Description of all turbine configurations and characteristic flow parameters

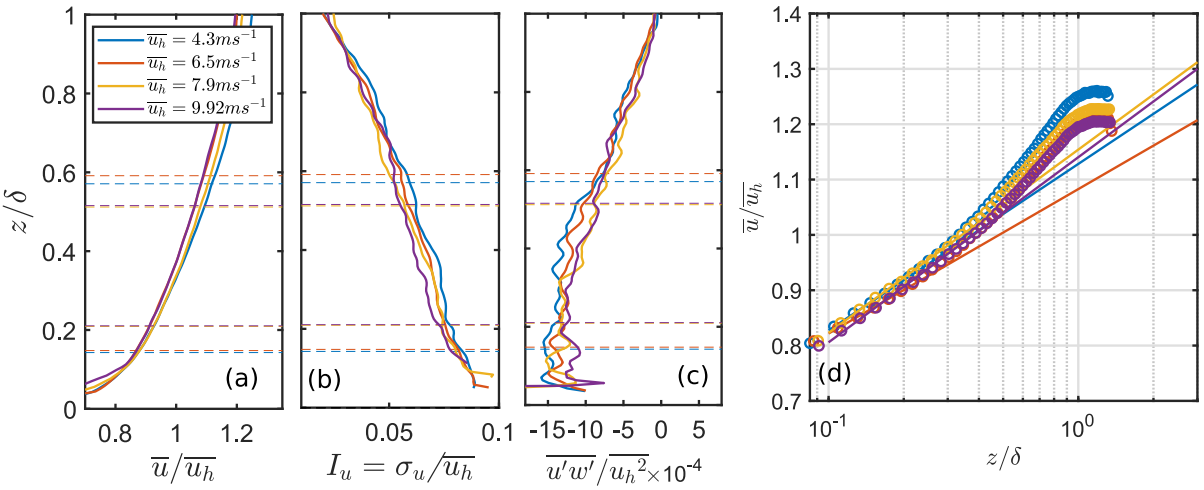

Figure 1. Vertical profiles of the normalized averaged streamwise velocity (a), streamwise turbulence intensity (b), normalized averaged vertical momentum flux (c), and normalized averaged streamwise velocity in logarithmic coordinates. The dashed horizontal lines in (a,b,c) represent rotor top and bottom limits, and the solid lines in (d) represent the logarithmic fit with experimental data in circles.

3. Results

3.1. Time-averaged wake characteristics

Figure 2 shows the contours of the normalized averaged streamwise velocity in the turbine wake for all the cases. The near wake velocity is observed to be significantly affected by the rotor diameter of the turbine, where the bigger rotor ($d = 15cm$) shows a lower $\overline{u}/\overline{u_h}$ than the smaller one ($d = 10.5cm$). A low-speed region emerging from the nacelle in the wake center can be observed in all cases. This is related to the wake of the nacelle, as noted by previous studies [21,22]. This region is observed to be stronger for the bigger rotor and plays a major role in the wake center velocity in the near wake. The near wake velocity appears to be independent of the nacelle diameter and rather depends on the nacelle length to rotor diameter ratio (l_N/d). The nacelle length to rotor diameter ratio is larger for the smaller rotor, indicating that a larger l_N/d leads to a higher wake velocity. The differences in the near wake velocity between different rotor diameters are observed to reduce with the increase in the Reynolds number. The wake of the tower can also be observed, which is stronger in the case of the smaller rotor due to a larger gap between the bottom tip of the rotor and the ground.

A more quantitative comparison of the normalized averaged streamwise velocity is shown in figure 3. Close to the turbine at $x/d = 0.5$, the smaller rotor with the two nacelle combinations shows a higher velocity than the bigger rotor at the smaller Reynolds number, indicating the aforementioned flow speed-up over the nacelle. For the higher Reynolds number, both rotors show a similar velocity profile. Further downstream, in the near wake ($x/d < 4$), a low-velocity region is observed at the hub height corresponding to the nacelle wake. The differences in the velocity profiles are higher for the lower Reynolds number in the near wake. In the far wake ($x/d \geq 4$), on the other hand, the velocity profiles are observed to converge to a similar profile for all cases. This indicates that the differences in the wake velocity due to different turbine configurations disappear in the far wake of the turbine. It also shows that the far wake velocity is independent of the Reynolds number for the tested range of the Reynolds number.

Figure 4 compares the vertical profiles of streamwise turbulence intensity in the turbine wake for different turbine configurations. Close to the turbine, the cases with the smaller rotor diameter show a significantly higher streamwise turbulence intensity in the lower half of the rotor

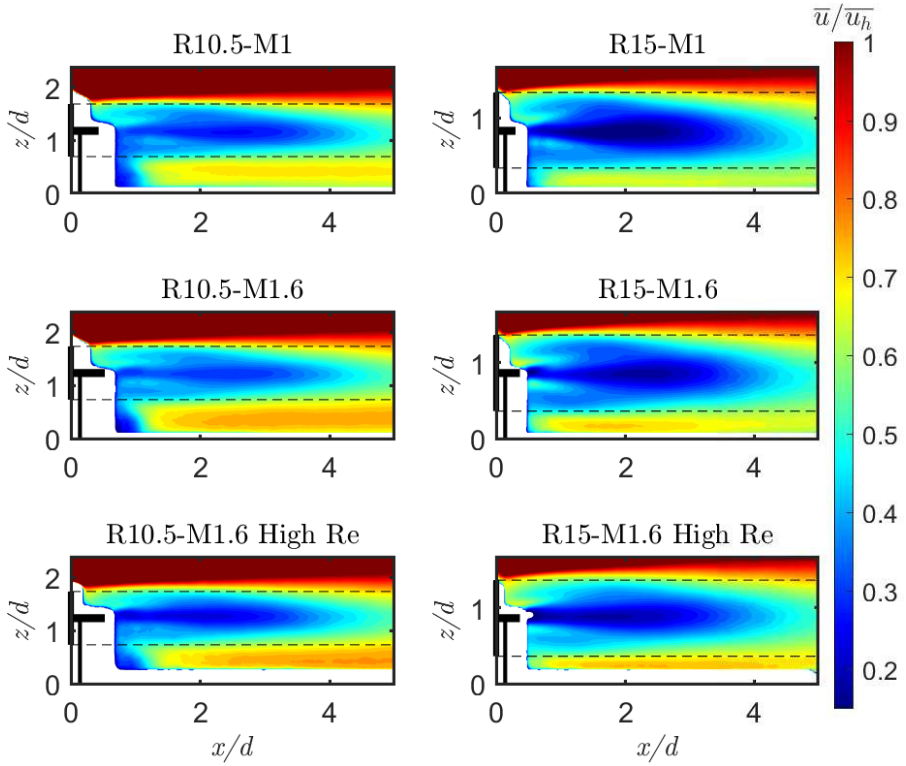

Figure 2. Contours of the normalized averaged streamwise velocity in the turbine wake.

projected area than the cases with the bigger rotor diameter. This can be associated with the effect of the turbine tower, which is more pronounced in cases with the smaller rotor diameter due to the larger clearance between the rotor bottom tip and the ground. At larger downstream distances ($x/d > 1$), all cases show similar turbulence intensity profiles. This indicates that the

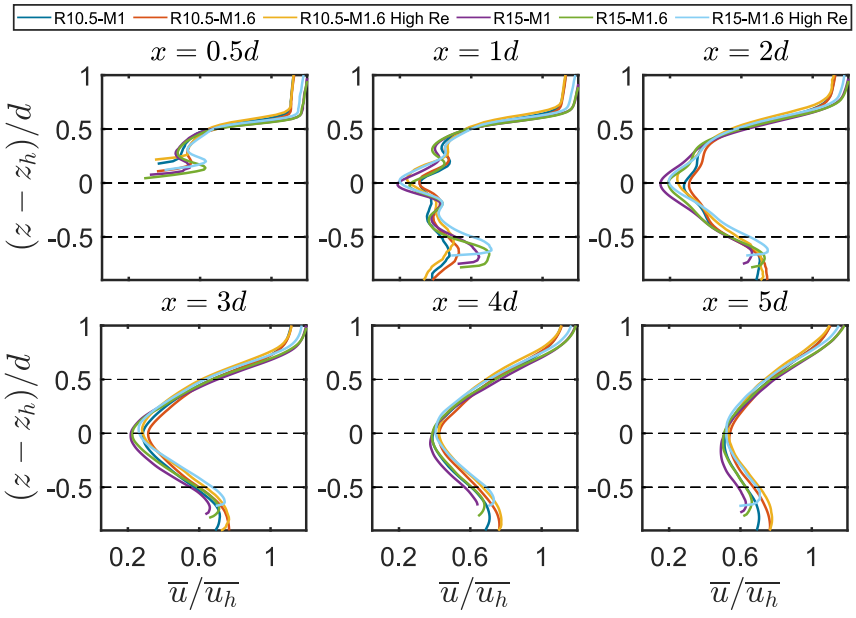

Figure 3. Vertical profiles of the normalized averaged streamwise velocity in the turbine wake at several downstream positions. The dashed horizontal lines represent the rotor tips and hub positions.

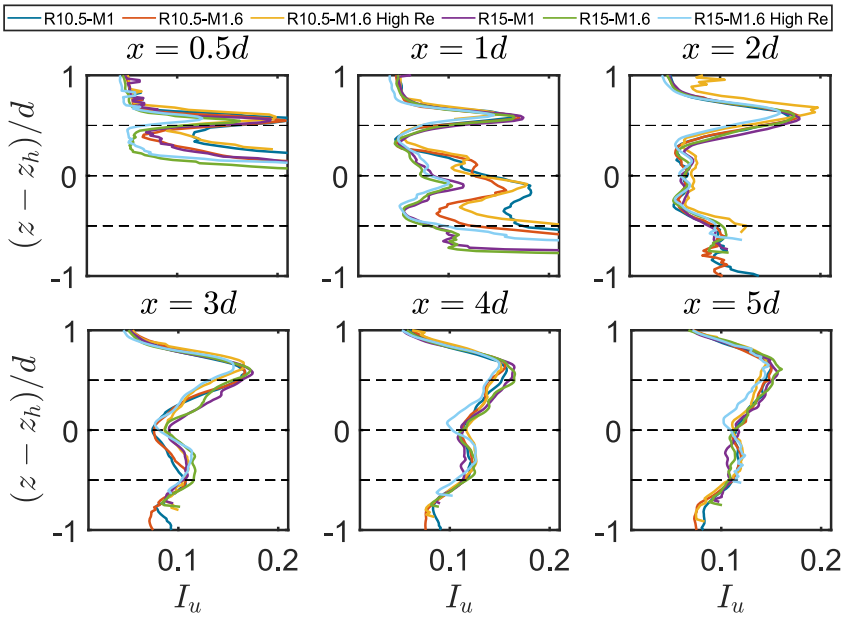

Figure 4. Vertical profiles of the streamwise turbulence intensity in the turbine wake at several downstream positions. The dashed horizontal lines represent the rotor tips and hub positions.

nacelle-to-rotor size only impacts the streamwise turbulence intensity close to the turbine. The high turbulence intensity close to the turbine at the hub height in the smaller rotor diameter can lead to an earlier breakdown of the hub vortex and is consistent with the higher normalized averaged streamwise velocity observed for the smaller rotor diameter cases.

We now compute the streamwise velocity deficit $\overline{\Delta u}$ as the difference between the incoming streamwise velocity and the streamwise velocity in the wake. Figure 5 compares the wake center velocity deficit identified by the maximum wake velocity deficit between different cases. An almost constant wake center velocity deficit can be observed at $x/d < 3$. As discussed in the literature [1, 23], in the near wake, the shear layer around the rotor periphery that exchanges energy between the wake and outer flow has not grown to re-energize the wake center. This is consistent with the near-constant wake center velocity deficit in the near wake observed in this study. In this region ($x/d < 3$), there are significant differences between the cases with different rotor diameters. However, cases with the same rotor diameter but different nacelle diameters show similar behavior. The wake center velocity deficit is observed to be higher for the cases with the bigger rotor ($d = 15cm$) than for the cases with the smaller one ($d = 10.5cm$). The difference between the cases reduces with the increase in the Reynolds number. Further downstream at $x/d > 3$, the normalized wake center velocity deficit converges to similar values for all the cases, indicating that the wake recovery in the far wake is not affected by the rotor or nacelle size.

3.2. Onset of far wake

In the previous section, we established that the near wake is significantly affected by the turbine configuration, whereas the flow statistics converged to similar values in the far wake. In this section, we evaluate the wake parameters characterizing the onset of the far wake. Understanding whether the nacelle-to-rotor size influences the onset of the far wake is important, as the onset parameters such as the near wake length and wake width at the start of the far wake are input parameters for most analytical wake models [1]. Figure 6 compares these parameters between different cases. The near wake length x_{nw} is obtained as the streamwise position where the experimental maximum normalized velocity deficit becomes equal to the theoretical maximum obtained from one-dimensional momentum theory [21]. The wake width at the end of the near

wake is computed as the standard deviation of a Gaussian profile fitted to the velocity deficit profile at the streamwise position corresponding to the end of the near wake. As can be observed, both the normalized near wake length and the normalized wake width at the start of the far wake show similar values for all the turbine configurations. This indicates that the nacelle and tower of a turbine do not have a significant effect on the transition from near to far wake.

3.3. Wake modeling

We now focus on analytically modeling the far wake velocity deficit for all turbine configurations. For this purpose, the Gaussian wake model proposed by Bastankhah & Porté-Agel [21] is used. According to this model, the normalized velocity deficit is estimated as:

$$\frac{\overline{u_\infty} - \overline{u_w}}{\overline{u_\infty}} = 1 - \sqrt{1 - \frac{\sigma_0^2 C_0(2 - C_0)}{\sigma(x)^2}} \times e^{-\left(\frac{r^2}{2\sigma(x)^2}\right)}, \tag{2}$$

where $\overline{u_\infty}$ is the averaged incoming flow velocity, $\overline{u_w}$ is the averaged wake velocity, C_0 is the maximum normalized velocity deficit at the start of the far wake obtained from the one-dimensional momentum theory ($1-\sqrt{1-C_T}$, where $C_T = 0.8$), σ_0 is the wake width at the start of the far wake and r is the radial distance from the wake center. The wake width σ in the far wake is obtained by the linear wake growth relation ($\sigma = k(x - x_{nw}) + \sigma_0$, where $k = 0.3I$ [24]).

Figure 7 compares the vertical profiles of normalized averaged velocity deficit obtained from the analytical model with that from the experiments. It can be observed that, despite different turbine configurations, the far wake deficit can be modeled with a consistent set of input parameters. This indicates that the variation in the nacelle-to-rotor size does not impact the far-wake modeling approach. This will allow the use of relatively large nacelle sizes for wake and power studies to reach larger Reynolds number without worrying about the nacelle effect on the modeling approach.

3.4. Power performance

The power coefficient of miniature turbines depends on the Reynolds number and the efficiency of the generator. Here, we compare the power coefficient obtained for all the turbine configurations at their optimal tip speed ratio. The power coefficient is computed as follows:

$$C_P = \frac{P}{0.5\rho A \overline{u_h}^3}, \tag{3}$$

where P is the total mechanical power computed as described earlier in equation 1, ρ is the air density and A is the rotor swept area.

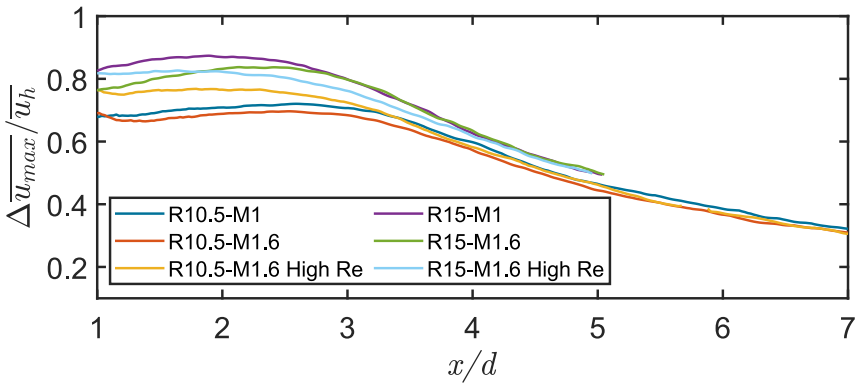

Figure 5. Comparison of the normalized averaged velocity deficit maximum between different cases.

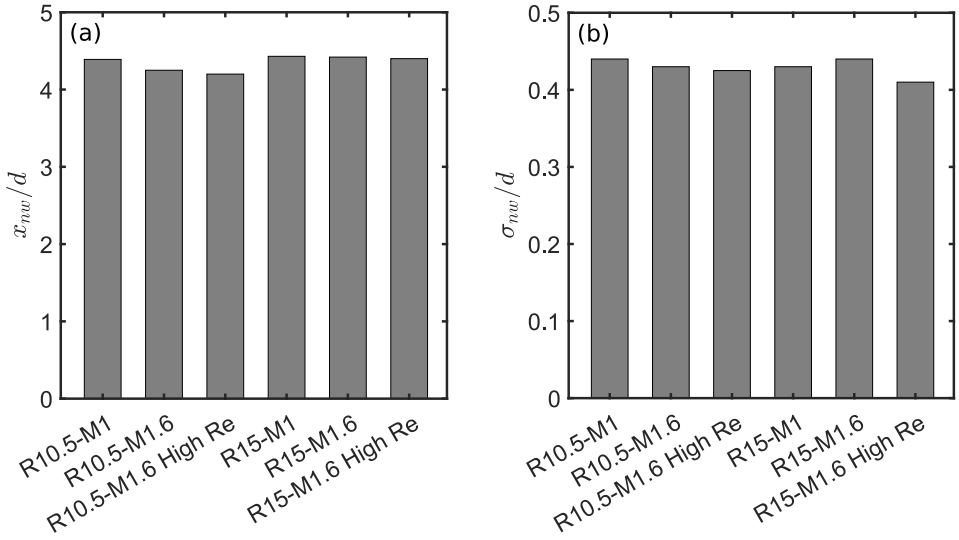

Figure 6. Bar plots comparing the normalized near wake length (a) and the normalized wake width at the end of the near wake (b) for different turbine configurations.

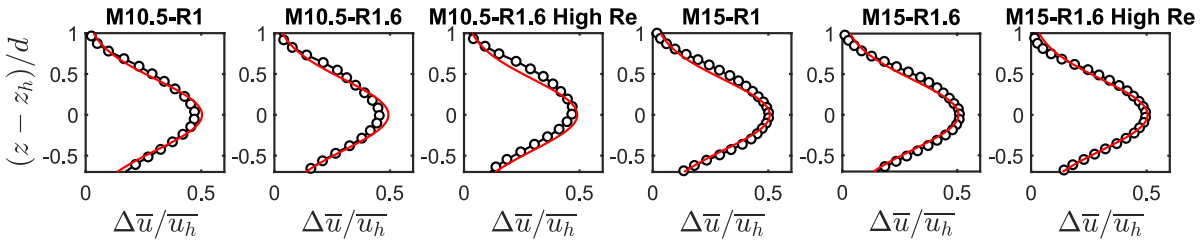

Figure 7. Comparison of the vertical profile of the normalized averaged streamwise velocity deficit at a downstream distance of $x = 5d$ between the experimental data (black line with markers) and analytical model (red solid line) for different turbine configurations.

Figure 8 compares the power coefficient obtained for all turbine configurations. It can be observed that, for a given motor and Reynolds number, both turbine rotor diameters yield a similar power coefficient. However, there is an improvement in the power coefficient between the DCX10L and DCX16L motors. In addition, with the increase in the Reynolds number, the power coefficient increases further reaching a value of approximately 0.4. This is an improvement of about 16% compared to the value for the smaller motor at a smaller Reynolds number. This highlights the importance of a higher Reynolds number, as well as a motor with better efficiency. Usually, the direct current motors have a limitation on the imposed current, which puts a limit on the Reynolds number. For the DCX10L motor used in this study, the Reynolds number is limited to around a value of 45000, whereas for the DCX16L, this value is around 75000. Therefore, using a bigger motor can help achieve a higher Reynolds number, which can result in a better power coefficient. In the future, a bigger motor can be used to achieve better turbine performance without worrying about its influence on the far wake characteristics and modeling parameters.

4. Discussion and Concluding Remarks

Miniature wind turbines used in wind tunnel experiments usually have large nacelle-to-rotor size ratios and lower Reynolds number compared to their utility-scale counterparts. For miniature

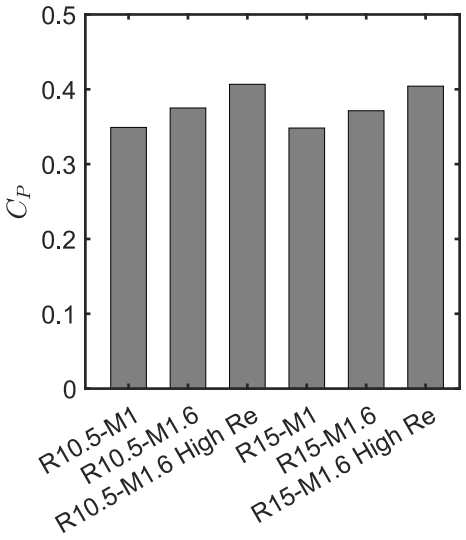

Figure 8. Comparison of the power coefficient between different turbine configurations.

wind turbines, the nacelle comprises a direct current motor, which is used to control the turbine and measure the power produced by it. These motors have a current limitation, which is usually associated with their size and limits the flow velocity up to which the turbine can be actively controlled (thereby affecting the Reynolds number). A larger motor can offer a higher current limit, and thus, enable controlled experiments at a high Reynolds number. The effect of nacelle-to-rotor size on the wake of a turbine is, however, not well understood in the literature. Wind tunnel experiments were performed using four different turbine configurations to investigate the effect of nacelle-to-rotor size ratios on the wake of a wind turbine under different Reynolds numbers.

The near wake velocity was observed to be significantly affected by the change in the rotor diameter, but not by the change in the nacelle diameter. This was consistent with the change in the nacelle length to rotor diameter ratio. The difference in the near wake characteristics reduced with the increase in the Reynolds number, whereas the onset of the far wake was unaffected by the nacelle-to-rotor size ratio. The far wake characteristics were unaffected by the nacelle-to-rotor size ratios, and the Gaussian wake model was able to predict the velocity deficit profile with good accuracy for all the cases. Finally, the power coefficient improved by 16% for the bigger motor (due to higher current limit) at a higher Reynolds number compared to that for the smaller motor at a lower Reynolds number.

In conclusion, this study showed that, in the most interesting region of a turbine wake i.e. the far wake, the nacelle-to-rotor size ratio does not have an influence. In addition, as the onset of the far wake is also unaffected by this ratio, the far wake modeling can be performed accurately. This will enable future experiments at higher Reynolds numbers with better turbine performance and without concerns regarding the effect of the blockage introduced by the turbine nacelle on the wake.

Conflict of Interest

The authors declare no conflict of interest.

Funding

This research was funded by the Swiss National Science Foundation (grant numbers: 200021_172538 and 200021_215288) and the Swiss Federal Office of Energy (grant number: SI/502135-01).

References

[1] Porté-Agel F, Bastankhah M and Shamsoddin S 2020 *Boundary-layer meteorology* **174** 1–59
[2] He R, Sun H, Gao X and Yang H 2022 *Renewable and Sustainable Energy Reviews* **166** 112675
[3] Krogstad P Å and Eriksen P E 2013 *Renewable energy* **50** 325–333
[4] Cal R B, Lebrón J, Castillo L, Kang H S and Meneveau C 2010 *Journal of renewable and sustainable energy* **2** 013106
[5] Bastankhah M and Porté-Agel F 2017 *Energies* **10** 923
[6] Dar A S, Armengol Barcos G and Porté-Agel F 2022 *Renewable Energy* **193** 1049–1061
[7] Bossuyt J, Scott R, Ali N and Cal R B 2021 *Journal of Fluid Mechanics* **917** A3
[8] Li Q, Murata J, Endo M, Maeda T and Kamada Y 2016 *Energy* **113** 1304–1315
[9] Dou B, Guala M, Lei L and Zeng P 2019 *Applied energy* **242** 1383–1395
[10] Abraham A, Dasari T and Hong J 2019 *Journal of Wind Engineering and Industrial Aerodynamics* **193** 103981
[11] Gaertner E, Rinker J, Sethuraman L, Zahle F, Anderson B, Barter G E, Abbas N J, Meng F, Bortolotti P, Skrzypinski W *et al.* 2020 Iea wind tcp task 37: definition of the iea 15-megawatt offshore reference wind turbine Tech. rep. National Renewable Energy Lab.(NREL), Golden, CO (United States)
[12] Limacher E J, Ding L, Piqué A, Smits A J and Hultmark M 2022 *Journal of Fluid Mechanics* **949** A24
[13] Santoni C, Carrasquillo K, Arenas-Navarro I and Leonardi S 2017 *Wind Energy* **20** 1927–1939
[14] De Cillis G, Cherubini S, Semeraro O, Leonardi S and De Palma P 2021 *Wind Energy* **24** 609–633
[15] Guo T, Guo X, Gao Z, Li S, Zheng X, Gao X, Li R, Wang T, Li Y and Li D 2021 *Applied Energy* **303** 117590
[16] Regodeseves P G and Morros C S 2021 *Energy Conversion and Management* **237** 114110
[17] O'brien J, Young T, Early J and Griffin P 2018 *Journal of Wind Engineering and Industrial Aerodynamics* **176** 32–53
[18] Zhu X, Sun C, Ouyang H and Du Z 2022 *Energy* **238** 121782
[19] Dar A S and Porté-Agel F 2020 *Journal of Physics: Conference Series* vol 1618 (IOP Publishing) p 062045
[20] Bastankhah M and Porté-Agel F 2017 *Energies* **10** 908
[21] Bastankhah M and Porté-Agel F 2016 *Journal of Fluid Mechanics* **806** 506–541
[22] Zong H and Porté-Agel F 2020 *Journal of Fluid Mechanics* **889** A8
[23] Neunaber I, Hölling M, Stevens R J, Schepers G and Peinke J 2020 *Energies* **13** 5392
[24] Brugger P, Fuertes F C, Vahidzadeh M, Markfort C D and Porté-Agel F 2019 *Remote Sensing* **11** 2247